Spatial Correlation Increase in Single-Sensor Satellite Data Reveals Loss of Amazon Rainforest Resilience

Lana L. Blaschke[1,2] , Da Nian[2], Sebastian Bathiany[1,2] , Maya Ben-Yami[1,2] , Taylor Smith[3], Chris A. Boulton[4], and Niklas Boers[1,2,4,5]

[1]Earth System Modeling, School of Engineering and Design, Technical University of Munich, Munich, Germany, [2]Potsdam Institute for Climate Impact Research, Potsdam, Germany, [3]Institute of Geosciences, University of Potsdam, Potsdam, Germany, [4]Global Systems Institute, University of Exeter, Exeter, UK, [5]Department of Mathematics, University of Exeter, Exeter, UK

Abstract The Amazon rainforest (ARF) is threatened by deforestation and climate change, which could trigger a regime shift to a savanna-like state. Whilst previous work has suggested that forest resilience has declined in recent decades, that work was based only on local resilience indicators, and moreover was potentially biased by the employed multi-sensor and optical satellite data and undetected anthropogenic land-use change. Here, we show that the average correlation between neighboring grid cells' vegetation time series, which is referred to as spatial correlation, provides a more robust resilience indicator than local estimations. We employ it to measure resilience changes in the ARF, based on single-sensor Vegetation Optical Depth data under conservative exclusion of human activity. Our results show an overall loss of resilience until around 2019, which is especially pronounced in the southwestern and northern Amazon for the time period from 2002 to 2011. The results from the reliable spatial correlation indicator suggest that in particular the southwest of the ARF has experienced pronounced resilience loss over the last two decades.

Plain Language Summary The Amazon rainforest (ARF) is Earth's most biodiverse ecosystem, crucial for regulating global and regional climate through water recycling and carbon uptake. Several studies suggest that ongoing deforestation, land-use changes, and climate change induced shifts in rainfall patterns could trigger an abrupt regime shift from the current rainforest to a low-treecover state. Here, we investigate the resilience of the ARF vegetation based on remotely sensed Vegetation Optical Depth, particularly useful in high-biomass areas such as the ARF. The main feedback mechanism, essential for potential tipping, is moisture recycling. The trade winds bring in moisture from the Atlantic Ocean to South America's east, where it precipitates. Much of this moisture re-enters the atmosphere via evapo-transpiration and is transported further west, thereby establishing a moisture regime supporting the rainforest. The induced spatial coupling results in the spatial correlation being a reliable indicator of resilience. We compare changes in the spatial correlation to changes in the two classic indicators. The greatest resilience loss is detected in the southwestern Amazon, which has been identified as a highly-coupled sub-system since it is reliant on recycled moisture from upstream the trade winds, hence making the spatial correlation a particularly suitable and trustworthy resilience indicator there.

1. Introduction

The Amazon rainforest (ARF) is the most biodiverse region of our planet, and serves as a major carbon sink (Gatti et al., 2021; Malhi et al., 2008). The ARF's important role in the global carbon cycle means that its existence and stability are crucial for climate change mitigation (IPCC, 2022). Yet, the efficiency of its carbon uptake has been declining over the last decades (Brienen et al., 2015; Gatti et al., 2021; Hubau et al., 2020; Malhi et al., 2008), with the ARF becoming carbon neutral and even acting as a carbon source during the two one-in-a-century droughts in 2005 and 2010 (Feldpausch et al., 2016; Gatti et al., 2014; Phillips et al., 2009).

Studies suggest that there is a critical mean annual precipitation (MAP) value at which parts of the forest might die, resulting in an irreversible and abrupt transition into a savanna-like state (Hirota et al., 2011; Zemp, Schleussner, Barbosa, Hirota, et al., 2017). In such a scenario, forest dieback would likely be self-amplifying, that is, the non-linearity of such a critical transition would result from positive feedback mechanisms. Besides fire (Brando et al., 2014), the main feedback mechanism that could amplify dieback in the ARF is related to moisture recycling (Salati et al., 1979; Staal et al., 2018). The dominant mechanism as well as its strength would determine

Writing – review & editing: Lana
L. Blaschke, Da Nian, Sebastian Bathiany,
Maya Ben-Yami, Taylor Smith, Chris
A. Boulton, Niklas Boers

the spatial extent of the transition. While fire-related dieback might stay confined locally, critical transitions associated with moisture-recycling can act on regional to continental scales (Bochow & Boers, 2023; Boers et al., 2017; Parry et al., 2022; Wuyts & Sieber, 2023). Moisture-recycling is initiated when moisture is transported via the low-level trade winds from the tropical Atlantic to the Amazon basin, where it precipitates. A substantial fraction is taken up by the vegetation and transpired back to the atmosphere, or evaporates from the complex surfaces of plants. This evapotranspired water is then transported further west and south over the Amazon and toward the Andes by the trade winds (Gimeno et al., 2016). The low-level circulation itself is amplified by condensational latent heating over the Amazon basin, strengthening the large-scale atmospheric heating gradient between ocean and land (Boers et al., 2017).

Two main external forcing mechanisms have been proposed that may activate positive feedback cycles and push the ARF toward a critical threshold (Lovejoy & Nobre, 2018, 2019). On the one hand, anthropogenic global warming will cause increased temperatures over the Amazon basin, which could lead to increased evapotranspirative demand without a corresponding increase in water supply via precipitation, especially during a potentially intensifying and prolonging dry season (Malhi et al., 2009) and severe droughts (Vogel et al., 2020). This could additionally lead to decreased convection and a reduction of moisture inflow from the Atlantic (Pascale et al., 2019); moreover, models from the Coupled Model Intercomparison Project Phase 6 (CMIP6) project an overall drying in tropical South America in response to increasing atmospheric greenhouse gas concentrations. Hence, global warming could drive the system toward destabilization (Zemp, Schleussner, Barbosa, Hirota, et al., 2017). On the other hand, deforestation can also lead to a critical decrease of evaporated moisture transported downstream, and to an additional reduction of moisture inflow due to a decreased heating gradient, further pushing the ARF toward a critical threshold (Bochow & Boers, 2023; Boers et al., 2017; Zemp, Schleussner, Barbosa, & Rammig, 2017). The decrease in precipitation that would occur beyond such a threshold would also cause degradation outside the ARF region.

Such vegetation carbon losses have been predicted by several CMIP6 models in parts of the Amazon basin, preceded by an increasing amplitude of seasonal temperatures (Parry et al., 2022). Furthermore, observations have shown that the Amazonian dry season is increasing in length (Leite-Filho et al., 2019; Marengo et al., 2017; Phillips et al., 2009), exacerbated by the three severe droughts that have occurred since 2005 (Feldpausch et al., 2016). In view of these projected and observed trends and the global relevance of the ARF, monitoring changes in its resilience is of great importance.

As the data-driven anticipation of critical transitions is important for many parts of our climate, and in particular the ARF, a considerable amount of research has focused on developing and applying such methods. The abruptness of a critical transition suggests that the mean state might not change noticeably before the transition happens. Thus, existing methods focus on the detection of distinct signs of resilience loss, where resilience is defined as a system's ability to recover from perturbations; the underlying mathematical concept is commonly termed critical slowing down (CSD) and is derived from dynamical system theory. Under the assumption that resilience loss can be dynamically represented by an approaching (codimension-1) bifurcation, the approach to the critical forcing value at which the bifurcation happens is accompanied by a weakening of the equilibrium restoring forces in the system. Accordingly, the system then becomes slower in recovering from small perturbations. During CSD, the variance and lag-1 autocorrelation (AC1) of the system's state variable increase, as they are directly linked to the recovery rate from perturbations (Boers et al., 2022; Dakos et al., 2008, 2012; Scheffer et al., 2009). Yet, in the case of spatio-temporal data, calculating the variance and AC1 at individual point locations does not exploit the information that is potentially encoded in the spatial dimensions, and in particular in the interactions between different locations. Dakos et al. (2010) argued that when a system consists of several coupled units, a decrease in the units' recovery rates causes increasing correlation between two coupled cells' state variables. To increase the readability, we will use the terms variance and AC1 without the reference to the state variable that shows the corresponding statistical property. Likewise, we will use the term "spatial correlation" to refer to the average correlation of the state variable at a given location with the state variable of neighboring cells, within a certain radius.

Smith et al. (2022) compared theoretical estimates of the recovery rates based on classical CSD indicators to direct estimates of the recovery rate from sections of remotely sensed vegetation time series that experienced abrupt disturbances. Thereby, they empirically confirmed Variance and AC1 to quantify resilience at global scale. Recent results by Boulton et al. (2022) have revealed that large parts of the ARF's vegetation biomass show
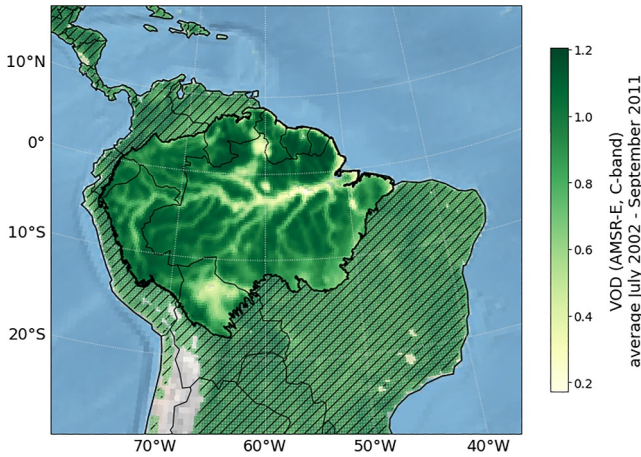
Figure 1. Average Vegetation Optical Depth in the Amazon basin measured by the C-band of the AMSR-E satellite sensor. Daily data is aggregated to a monthly resolution by taking the mean over complete months, hence the time period from July 2002 to September 2011 is considered in the case of AMSR-E. The outline of the Amazon basin can be found at https://worldmap.maps.arcgis.com/home/item.html?id=f2c5f8762d1847fdbcc321716fb79e5a.

increasing AC1, implying a loss of resilience that has been especially pronounced since the early 2000s. Both the study of Smith et al. (2022) and Boulton et al. (2022) used multi-satellite data to extend the period of time under study (Moesinger et al., 2020). Yet, Smith et al. (2023) subsequently showed that such merging of sensors can create spurious changes in higher-order statistics such as variance and AC1 when those are calculated from multi-instrument time series. The non-stationarity induced in the time series by the change of sensors, orbits, intrinsic noise, and radiometric resolutions may result in statistical signals which can be misinterpreted as resilience changes. It is thus recommended to investigate the resilience changes in a system by using single-sensor instrument records when available. In this work we thus exclusively use single-sensor data: in particular, Amazon vegetation indices based on Vegetation Optical depth (VOD), see Figure 1. While indicators of CSD could react differently to changes in the measurement process or to systemic changes that are not related to CSD, different indicators that are related to CSD via the recovery rate should behave consistently whenever the resilience changes. We thus ensure the robustness of our results by comparing the trends of calculated spatial correlation to corresponding trends of the AC1 and variance. To further ensure robustness, we compare different data sources as recommended by Samanta et al. (2012).

To test the validity of different CSD indicators for spatially coupled systems, we also test and compare them using simulations from a conceptual one-dimensionel moisture recycling model. It has been suggested that different areas of the ARF can be considered part of a coupled system, connected by spatial interactions via moisture recycling, involving evapotranspiration, winds, and precipitation (Staal et al., 2018). Hence, the ARF's vegetation interacts indirectly via precipitation, as opposed to direct interactions of the state variables with each other, and these interactions are nonlinear and encompass a large range of scales. These interactions mainly occur along the wind direction since moisture is advected downstream by the mean circulation. Moreover, the circulation itself can also be affected by surface roughness and albedo. Thus, it is not immediately obvious whether increasing spatial correlations between the grid cells' vegetation as introduced by Dakos et al. (2010) would occur, since Dakos et al. (2010) modeled interactions solely via diffusion. To ensure the reliability of the different CSD indicators, including the spatial correlation, we first test them on a conceptual model that comprises the above mentioned peculiarities. Since the trade winds transport moisture from east to west, we assume that coupling cells in one direction is a reasonable simplification of the plant-water moisture transport system in the Amazon (Boers et al., 2017). Ideally, the flows can be investigated as separated trajectories (like in a laminar flow), thereby allowing a reduction to one dimension (Boers et al., 2017). Based on this reduction, we set up a simple conceptual model with asymmetric interaction (see Figure 2.) to validate and compare the performance of variance, AC1, and spatial correlation as
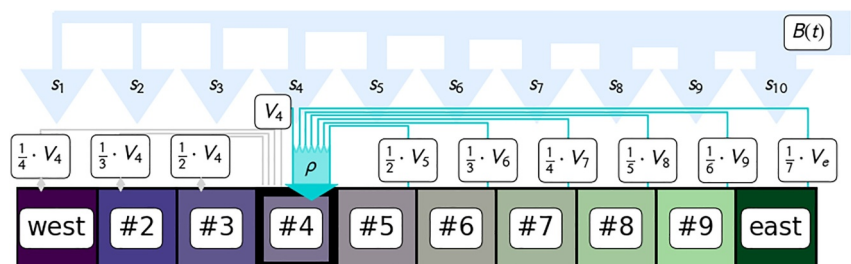
Figure 2. Conceptual moisture recycling model. The thin turquoise arrows represent the incoming precipitation due to moisture recycling and the thick light blue arrows indicate the precipitation directly originating from the Atlantic ocean. For each cell i, a scaling factor s_i determines the fraction of "background precipitation" $B(t)$ that precipitates. As an example, cell #4 and its corresponding incoming and outgoing fluxes are highlighted. Each cell to the east of cell #4 contributes by $(d_i + 1)^{-1} V_i$ where d_i is the model distance between cell i and cell #4 and V_i is the vegetation content in cell i. Thin gray arrows mark the precipitation in other cells that originated from cell #4. The decrease of the control parameter $B(t)$ representing the overall incoming moisture from the Atlantic induces a critical transition in the vegetation model.

indicators of CSD and, hence, resilience loss of vegetation in a setting like the ARF. Subsequently, we calculate all three resilience indicators for four single-sensor VOD satellite data sets, which quantify the ARF's vegetation proxy of above-ground water content in biomass. Finally, based on these results we discuss changes in resilience of the ARF.

2. Materials and Methods

2.1. Description and Parametrization of the Conceptual Model

To demonstrate the relevance of the three indicators of CSD in a setting like the ARF, with indirect and asymmetric coupling between multiple grid cells, we slightly modify a previously introduced conceptual model of atmosphere-vegetation interaction (Bathiany et al., 2013a). The vegetation dynamics of the model are inspired by the global dynamical vegetation model VECODE (Bathiany et al., 2013b; Brovkin et al., 1997, 1998, 2002), which is based on an empirical relationship of vegetation cover fraction and atmospheric conditions.

In particular, the equilibrium vegetation V^* is a monotonic (sigmoidal) function of precipitation (see Equation 1). The vegetation dynamics are simulated as a linear relaxation toward this empirical equilibrium. The general equilibrium vegetation $V^*(P)$ is a direct function of total incoming precipitation P_i in [mm/year], namely

$$V^* = \begin{cases} 0 & \text{if } P_i < P1 \\ 1 & \text{if } P_i > P2 \\ 1.03 - 1.03\left(1 + \dfrac{\alpha}{\exp(\phi)^2}(P_i - P1)^2\right)^{-1} & \text{otherwise.} \end{cases} \tag{1}$$

here, P_i represents the amount of precipitation in a cell i, as the spatial extension of our model consists of 10 cells. Both, α and ϕ, are model parameters. While VECODE is based on an empirical relationship of vegetation cover fraction based on atmospheric conditions, we here interpret the vegetation variable V^* as a property linked to the tree cover in the Amazon (e.g., tree cover fraction or biomass). We motivate this interpretation by the following. First, the nature of the model approach is highly conceptual. Second, tree coverage in the original VECODE version is modeled by a very similar approach as vegetation coverage (with a curve that is shifted to higher precipitation rates). Making the model more complex by distinguishing plant types would hence not add to our analysis.

The parameters $P1$ and $P2$ in Equation 1 are given by

$$\begin{aligned} P1 &= \beta \cdot \exp\left(\frac{\phi}{2}\right) \\ P2 &= \beta \cdot \exp\left(\frac{\phi}{2}\right) + \frac{\exp(\phi)}{\sqrt{0.03\alpha}}. \end{aligned} \tag{2}$$

The parametrization is chosen in a similar way to Bathiany et al. (2013a) but adapted such that the range of bistability in dependence of precipitation is closer to that in the ARF. Namely, the parameters are $\alpha = 0.0011$, $\beta = 280$, and $\phi = 2.45$. Thus, the vegetation $V_i \in [0, 1]$ of a cell i at time $t + 1$ is given by

$$V_i^{t+1} = V_i^t + \frac{V^*(P_i^t) - V_i^t}{\tau}\Delta t, \tag{3}$$

where P_i^t is itself a function of the vegetation state V^t. Specifically, following Bathiany et al. (2013a), we implement an atmosphere-vegetation feedback in our model by forcing the precipitation with the vegetation. This installs the moisture-advection feedback as the coupling mechanism, and can in principle capture many land surface mechanisms. Nevertheless, with this focus, the resulting feedback mechanisms can then be considered to act uni-directionally from east to west following the fluxes in the atmosphere over the Amazon (Salati et al., 1979; Staal et al., 2018). Thus, the cells can be thought as a row along a trade wind trajectory, with cell #1 representing the most downstream region (southwestern Amazon) and cell #10 the eastern-most cell (East coast of South

America). Then, the precipitation from moisture recycling $P_i^{recycled}$ is a sum of vegetation in the cells to the east of cell i (cells with higher indices $j \geq i$), weighted by the model distances. Mathematically, it can be expressed as

$$P_i^{\text{recycled}} = \rho \cdot \sum_{j \geq i} \frac{1}{j - i + 1} \cdot V_j \tag{4}$$

and acts a coupling between the cells. The scaling factor ρ is set to 600. Note that each cell's recycled precipitation is also dependent on its own vegetation cover V_i. Additionally, in each cell the precipitation depends on the amount of moisture that arrives from the Atlantic ocean, which is represented by the control parameter B. This background precipitation is the product of a scaling factor s_i times $B(t)$. The scaling factor

$$s_i = \max\{0.1 \cdot i, \ 0.2\}$$

models the amount of precipitation that results directly from the ocean. Hence, it is highest in the east ($s_{10} = 1.0$) and decreases toward the west ($s_1 = s_2 = 0.2$). In summary, the total precipitation in cell i is a sum of background precipitation and precipitation $P_i^{recycled}$ from moisture recycling in the "east" of the cell and is given by

$$P_i = B \cdot s_i + P_i^{\text{recycled}} + \sigma \eta_i, \tag{5}$$

where the standard deviation of the additive white noise component $\eta_i \sim \mathcal{N}(0,1)$ is set to $\sigma = 20$. A visualization of the deterministic part of precipitation in the model is given in Figure 2.

To mimic a climate change scenario with declining moisture inflow from the Atlantic ocean, the bifurcation parameter B decreases linearly from 1010 to 990 over time in our model runs. One should note that due to the different magnitudes of moisture inflow from moisture recycling, the critical value of the control parameter B differs between the cells. The model's stability is explained in more detail in Text S1 in Supporting Information S1. It transitions to a low vegetation state once the critical threshold of precipitation is crossed. For more details on the stochasticity and abrupt change in precipitation, see also Text S2 in Supporting Information S1.

While the characteristic relaxation time in VECODE is climate dependent, we here follow Bathiany et al. (2013a) and set it to a constant value (here: $\tau = 100$ years), which allows a more straightforward interpretation of CSD in the model. The constant τ resembles the inherent timescale of the vegetation system. The time step $\Delta t = 1$ corresponds to 1 year in accordance with P representing mean annual precipitation. This is slightly different than our analysis and later sections of the paper, since the VOD observations are available for ∼10 years, with fluctuations happening on monthly scale. However, the time scale difference does not impact the results, as a time step unit could also be interpreted as for example, days or months.

Realizations of the model are obtained by numerically approximating the solutions of the given equations by an Euler-Maruyama-scheme. As this analysis focuses on measures that are valid in the vicinity of the fixed point, equilibrium runs are performed. For each change in the bifurcation parameter, 1000 steps of the Euler-Maruyama-scheme are executed, and the result of the last one is added to the data set as one time step. Moreover, the data of the first time step are the result of 10,000 steps with initial values randomly distributed around the fixed point. The simulations shown are based on 1000 time steps. All results are based on 1000 realizations of the stochastic model.

2.2. Resilience Analysis

To assess changes in resilience based on the concept of CSD, we de-trend and de-season the data sets and calculate the variance, AC1 and spatial correlation in sliding windows. The change is then defined as the time series' linear trends.

2.2.1. De-Trending and De-Seasoning

All indicators of CSD are based on perturbations of the state variable around its equilibrium. Hence, the analyzed time series must not contain any trend or seasonality. For the conceptual model, this is achieved by subtracting the

equilibrium vegetation state of the corresponding cell from its vegetation state in each realization. For the satellite vegetation data, the trend and seasonality of each time series are removed separately by applying the Seasonal-Trend decomposition using LOESS (STL). The parameters are set to the default values proposed by Cleveland et al. (1990) for the analysis in the main text, but the results are robust against variation in the parametrization, see Text S3 in Supporting Information S1.

2.2.2. Detection of Resilience Changes

The classical indicators variance and AC1 are calculated grid-cell-wise. What is referred to as *spatial correlation* is the average temporal correlation of the time series of a cell i's state variable with its neighbors' time series. Note that correlation refers to the Pearson correlation coefficient throughout this study. The spatial correlation at a grid cell i can be written as

$$C_i = \frac{1}{n}\sum_j Cor(r_i, r_j) \qquad \text{for} \qquad j \in \Omega_i,$$

where r_i and r_j are the detrended time series in the grid cells i and j. The neighborhood Ω_i comprises n cells defined as neighbors of cell i. In the conceptual model only the one or two directly neighboring cells to the east and west are considered when computing a cell's spatial correlation value. For the observational data, the neighborhood Ω_i is defined as all cells within a given radius of cell i. The radius is 100 km for the main results, a scale on which moisture recycling is highly influential (Staal et al., 2018). However, the results are robust against other choices (see Text S4 in Supporting Information S1). All distances are calculated based on the great circle distance between grid cell centers. In the conceptual model, we only consider neighbors to the east and west, while for the satellite data the radius defines the neighborhood, thus also taking cells to the north and south into account. We believe that the conceptual model is still a reasonable approximation of the situation, since the large-scale atmospheric flow in reality has one specific direction at any point in time, so adding the second dimension should not change the overall behavior of CSD indicators.

To evaluate the change in resilience over time, we examine the development of the corresponding indicators of CSD over time. Thus, the indicators are not calculated on the complete time series but on windows that are sliding across the time series. In particular, for a time series $[t_1, t_2, \ldots t_N]$ the jth window of size w is $[t_j, t_{j+1}, \ldots, t_{j+w}]$ with $j \in 1, \ldots, N - w$. For the conceptual model, the size of the windows is set to 100 time steps. In the real data, defining the sliding window size must be done with consideration of the total length of the time series. Large window sizes ensure robust indicator values, but leave less time steps to calculate their corresponding trends or tendencies. In the main analysis, the window size is 5 years, equivalent to 60 data points. The trade-off is especially high in the case of the single-sensor data considered here due to their short availability. Yet, the results are robust with regards to the window size (see Text S5 in Supporting Information S1).

The change of the resulting indicator time series is then quantified by the trend, which is defined as the slope of a linear regression. However, the trend could be biased by large jumps in the time series. We thus also use the Kendall τ correlation coefficient, which assesses the time series' tendency, measured as the steadiness of the increase. In the main text, all results are stated in terms of trends, but are robust when compared to results assessed by the tendency (see Text S6 in Supporting Information S1).

2.2.3. Time of Emergence

To assess the performance of the different indicators, we define the time of emergence (ToE) as the time a statistically significant trend emerges in the corresponding indicator time series for the first time. To calculate the ToE for the conceptual model, we create 1,000 surrogates by running the model with constant $B(t) \equiv 1,000$, corresponding to the null model assumption that the system does not move toward the bifurcation point. We then re-run the CSD analysis on these surrogates. For each time step, the trend in the surrogate's indicators as well as in the original state variable's indicators is measured until this point in time. This gives null model distributions for each cell and time step. An indicator's instance at a given time and cell is regarded as significant if its trend is above the 95th percentile of the corresponding null model distribution, that is, if $p < 0.05$. The ToE is then defined as the first time when the trend has $p < 0.05$. The ToE was similarly defined for example, by Hawkins and Sutton (2012) as the first time a signal-to-noise ratio is above a certain threshold. An indicator of CSD used as an

Early Warning Sign (EWS) should preferably warn as early as possible. Thus, indicators are better the earlier their increase is significant before a tipping point. Furthermore, they are more reliable when the spread in the ToE over the realizations is small.

2.3. Data

Remote sensing of high biomass regions such as the ARF is challenging for several reasons. For example, Vegetation Indices (VIs) based on optical imaging may fail due to a dense canopy, which can lead to asymptotic saturation (Huete et al., 2002). Moreover, artifacts from persistent cloud cover and aerosols may remain in the processed VI (Samanta et al., 2012). In contrast, VOD (Jackson & Schmugge, 1991; Vreugdenhil et al., 2016) is derived from microwave satellite observations and linked to vegetation water content (Kirdiashev et al., 1979) via which it can be interpreted as an indicator of canopy density and above-ground-biomass. Smith et al. (2022) showed that at the global scale VOD is more suitable for a vegetation resilience analysis based on CSD. Besides the reliability of the VI, sufficiently long time series are crucial for the analysis of the evolution of vegetation resilience. Yet, while long-time scale merged VOD products exist (e.g., VODCA (Moesinger et al., 2020)), intercalibration techniques in multi-sensor observational products providing long time series can cause artifacts in any resilience analysis that is based on CSD (Smith et al., 2023). Hence, here we analyze only single-sensor data, all of which was recorded over a time span of at least 8 years. For the time period from 2000 to 2020 two sensors recorded suitable data. First, the Advanced Microwave Scanning Radiometer Earth Observing System sensor (AMSR-E) (Vrije Universiteit Amsterdam (Richard de Jeu) and NASA GSFC (Manfred Owe), 2011) was active from June 2002 to October 2011. Since we process the daily data by taking averages over full months following (Boulton et al., 2022), only the time period from July 2002 to September 2011 is analyzed. AMSR-E provides VOD data based on the C- and X-bands. These bands stem from a sampling of frequencies around 6.9 and 10.7 GHz., respectively. In theory, higher frequencies (X-band) are mainly responsive to the moisture content of the canopy (Chaparro et al., 2018; Fan et al., 2018; Konings et al., 2019; Tian et al., 2018), while lower frequencies (C-band) are more sensitive to deeper vegetation layers, including the woody parts (Andela et al., 2013). AMSR-E's successor AMSR2 (Vrije Universiteit Amsterdam (Richard de Jeu) and NASA GSFC (Manfred Owe), 2014) was launched in July 2012 and is still active. In this sensor the C-band was divided into two frequency bands termed C1 and C2 (6.9 and 7.3 GHz), and VOD data can be derived from both. The first complete month of AMSR2 is August 2012, and due to the availability of the data used to exclude Human Land Use (HLU), AMSR2 is analyzed until December 2020.

To access the changes in the Amazon rainforest over these decades, we use the VOD data derived from the nighttime overpass recordings, as they are more suitable for VOD (de Jeu et al., 2008). The spatial resolution is kept at 0.25°.

2.4. Grid Cell Selection

To define natural rainforest grid cells within the Amazon basin (http://worldmap.harvard.edu/data/geonode: amapoly_ivb), two data sets are used to check for the following two requirements. A cell must have at least 80% evergreen broadleaf fraction (EBlF) and 0% human land use (HLU), extracted from the MODIS Land Cover data set (Friedl & Sulla-Menashe, 2015) (MCD12C1, Version 6), based on Land Cover Type 1 in percent. This data is available from 2001 until 2020. We define HLU as any of *Croplands*, *Urban and Built-up Lands*, and *Cropland/ Natural Vegetation Mosaics*. Thus, to avoid misinterpreting HLU changes after 2020 (DeArmond et al., 2023; INPE, 2023) as resilience changes, we only analyze pre-2020 years. In particular, Wang et al. (2024) recently showed that anthropogenic influence highly affects resilience in the ARF. Thus, to be as rigorous and conservative as possible, we also exclude any cell with more than one percent forest loss during 2001–2020, using the values from Hansen et al. (2013). The percentage refers to the accumulated area of forest loss detected over time. This data selection is visualized in Figure 3.

3. Results

3.1. Resilience Indicators in a Conceptual Model of Vegetation-Atmosphere Moisture Recycling

The conceptual model implements moisture-recycling from east to west in combination with decreasing moisture inflow from the Atlantic ocean. This latter effect corresponds to a potential climate change scenario and acts as the forcing in the model. Once the point is reached where the eastern cell tips to a low vegetation state, the abrupt
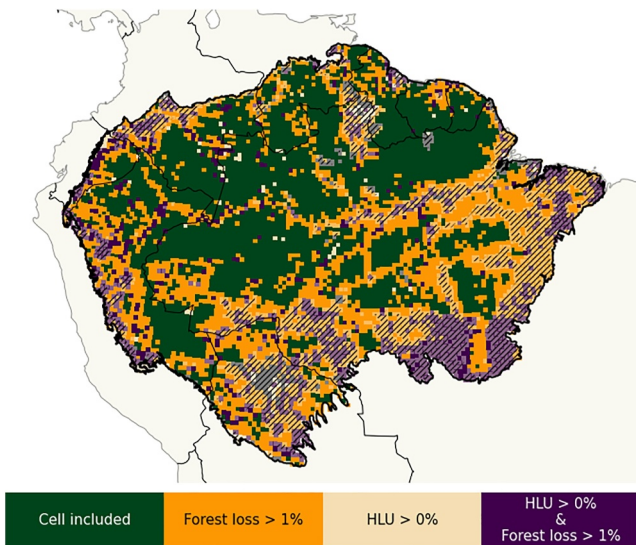
Figure 3. Grid cells included in the analysis. For a grid cell to be included (green), there may not be any remotely sensed Human Land Use (Friedl & Sulla-Menashe, 2015) (HLU, violet) and the forest loss according to Hansen (Hansen et al., 2013) (orange) may not cumulate to more than 1% of the cell's area over the years 2001–2020. Furthermore, the Evergreen Broadleaf Fraction (EBlF, hatched) may not be less than 80% in any of the years, assuring that only dense rainforest is considered.

decline in vegetation reduces the inflow of recycled moisture in all the cells further to the west, thus inducing a tipping cascade from east to west. The spread in the actual tipping point in Figure 4a is a result of stochastic differences between the realizations, owing to the white noise added to the precipitation. Before the tipping point, the resulting decline in precipitation is almost linear for all of the cells (compare the zoom-in into precipitation in Figure S2 in Supporting Information S1). Interestingly, deforestation in the eastern-most cell mimicked by an artificial linear reduction of this cell's vegetation state also induces a cascade of precipitation and vegetation tipping (see Text S7 in Supporting Information S1).

In Figure 4, the vertical black lines mark the last time step included in the CSD analysis, when no cell's realization has yet tipped. For all cells, variance, AC1 and spatial correlation as indicators of CSD are calculated on sliding windows of the simulated vegetation time series. For all indicators and all cells, the three indicators increase on average with almost no negative trends (see Text S8 in Supporting Information S1).

As defined in Section 2.2.3, the time of emergence (ToE) is the time when the trend of an indicator becomes significant for the first time. In Figure 4, the median ToE is highlighted by an orange line and differs both between different cells and between different indicators for the same cell. For all cells the spatial correlation outperforms the other indicators as an EWS in terms of the average ToE. Furthermore, an indicator is regarded more reliable when its trend consistently becomes significant at one time. This can be translated to a smaller spread in its ToE. For all cells, the variance exhibits the smallest
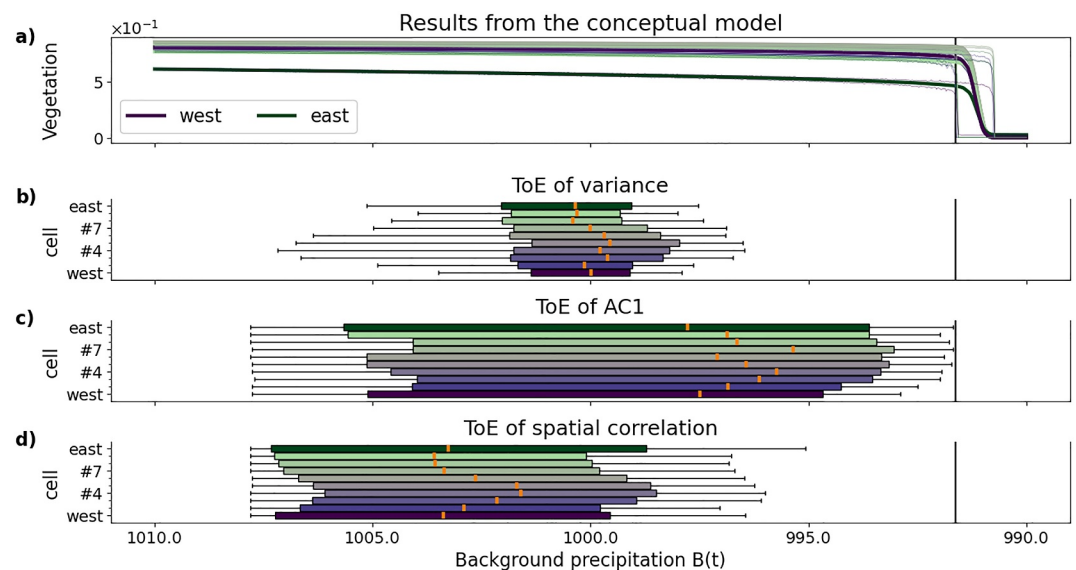

Figure 4. Performance of the three CSD-indicators across 1,000 realizations of the conceptual model. The upper panel (a) shows the modeled vegetation time series. Thick lines show the mean, while thin lines mark the maximum and minimum over all realizations. The vertical black line indicates the last time step still taken into account for the CSD analysis. The panels (b)–(d) show the CSD-indicators' times of emergence (ToE), that is, when the trend for a CSD-indicator first becomes significant for a given cell in one realization. Each boxplot shows the distribution across the realizations of the ToE of (b) variance, (c) AC1, and (d) spatial correlation. Since ToEs differ between cells, they are given for each cell individually, with the western-most cell being at the bottom of the y-axis and the eastern-most being on the top. In addition, colors encode the 10 cells as in Figure 2. The distributions' medians are highlighted in orange, while the boxes indicate the first to third quartiles. The 5th to 95th percentiles are visualized as whiskers. Since the background precipitation B(t) is reduced linearly with time, the x-axis corresponds to time as well as decreasing B(t).

spread. Yet, the variance is prone to biases that can result from data collection or changes in the system noise amplitudes, see for example, (Ben-Yami et al., 2023; Boers, 2021; Smith et al., 2023). Accordingly, in real data applications, it is likely to be less reliable as an indicator of CSD than it is in a theoretical model. In contrast, the spatial correlation is not only earlier but also more reliable than the AC1. However, any indicator can sometimes have spuriously significant trends that lose their significance at a later time, so it is informative to also define a "permanent" ToE. This ToE is defined as the time when the emergence of a significant trend is permanent for the rest of the time period, and is discussed in Text S9 in Supporting Information S1. While this definition reduces the large uncertainty in the ToE of AC1 and spatial correlation, using a permanent ToE does not alter the relations between the median ToEs of the different indicators. The overall result also stays the same: the spatial correlation is the earliest indicator to have significant positive trends. In addition, a Fourier approach to surrogates as investigated for example, by Ben-Yami et al. (2023) confirms the potential of spatial correlations as an EWS, especially in the coupled cells.

We conclude that, whilst their significance might emerge at different times, all three indicators are expected to increase for spatially extended systems like the ARF when approaching a critical transition. Moreover, the spatial correlation proves its reliability as an indicator of CSD in coupled systems. Consequently, if the ARF is losing resilience, we would expect coherent and significant increases in all three CSD indicators in observations of Amazon vegetation.

3.2. Vegetation Resilience in the Amazon Basin

As the ARF is a spatially coupled system, similar to the simple moisture recycling model presented above, we expect to see increasing indicators of CSD in case of resilience loss. Three indicators are considered here, namely variance, AC1, and spatial correlation. The change in an indicator's time series is quantified by the linear trend (see Methods section). Figure 5 displays the spatial pattern of trends in the individual indicators as found for the different data sets. It is important to keep the different time spans of the two sensors in mind, as the results can only be compared within each sensor's bands.

2002 - 2011 (AMSR-E): From July 2002 to September 2011, AMSR-E was active. The changes in the single indicators for AMSR-E's C- and X-band are depicted in Figures 5a–5f. For its C-band, the distributions of trends of all indicators have a positive median, so overall more cells exhibit a positive trend than not. Whilst the spatial distributions of trends in variance, AC1 and spatial correlation are distinct, in all three the positive trends cluster in the southwest and along the northern basin boundary. AMSR-E's X-band has, for all three indicators, an even stronger tendency toward cells with a positive trend. The regions of positive trends are similar to those of the C-band, but extend across the whole Amazon basin, with the only exceptions being some cells with non-positive trends in the east, close to the Amazon river.

As explained above, in the case of CSD we would expect the changes in all three indicators to be coherent. Figure 6 summarizes the results from the three indicators. The maps show the number of indicators exhibiting a positive trend at each grid cell. For AMSR-E's C-band, Figure 6a confirms that the most prominent patch of positive trends in all indicators is the southwestern part of the Amazon basin. Further signs of extended resilience loss are noticeable along the northern basin boundary. For the X-band, the overall resilience loss of the ARF, especially pronounced in the southwest, becomes apparent in Figures 6b and 6e. The time series of spatial averages suggest that the ARF as an interacting ecosystem has, on average, lost resilience over the years 2002–2011, with clear signals in both bands.

2012–2020 (AMSR2): Turning to the time period from August 2012 until December 2020, for which VOD data based on AMSR2 was analyzed, the signal is less clear (Figure 5). Even so, except for the AC1 of the C2-band, the trends of all indicators are more often positive than negative. As for AMSR-E, the two bands in AMSR2 have different spatial trend distributions. For the C1-band, patches of positive trends, mostly in the variance and spatial correlation, are visible in the northeast as well as in the west. For the C2-band, the signals are stronger in the west but less pronounced in the northeast, and again strongest in the variance and spatial correlation. The spatial comparison of the trends in the three indicators in Figure 6c reveals that, based on the C1-band, the vegetation in the northeast of the Amazon basin has lost resilience. Even though no clear signals in this region were found for the years 2002–2011 based on AMSR-E's C-band, its X-band does show destabilization in this region already in the years before 2012. The results from the C2-band show positive trends co-occurring mainly in the very west, where both bands from AMSR-E indicated a loss of resilience for the previous decade. The spatially averaged
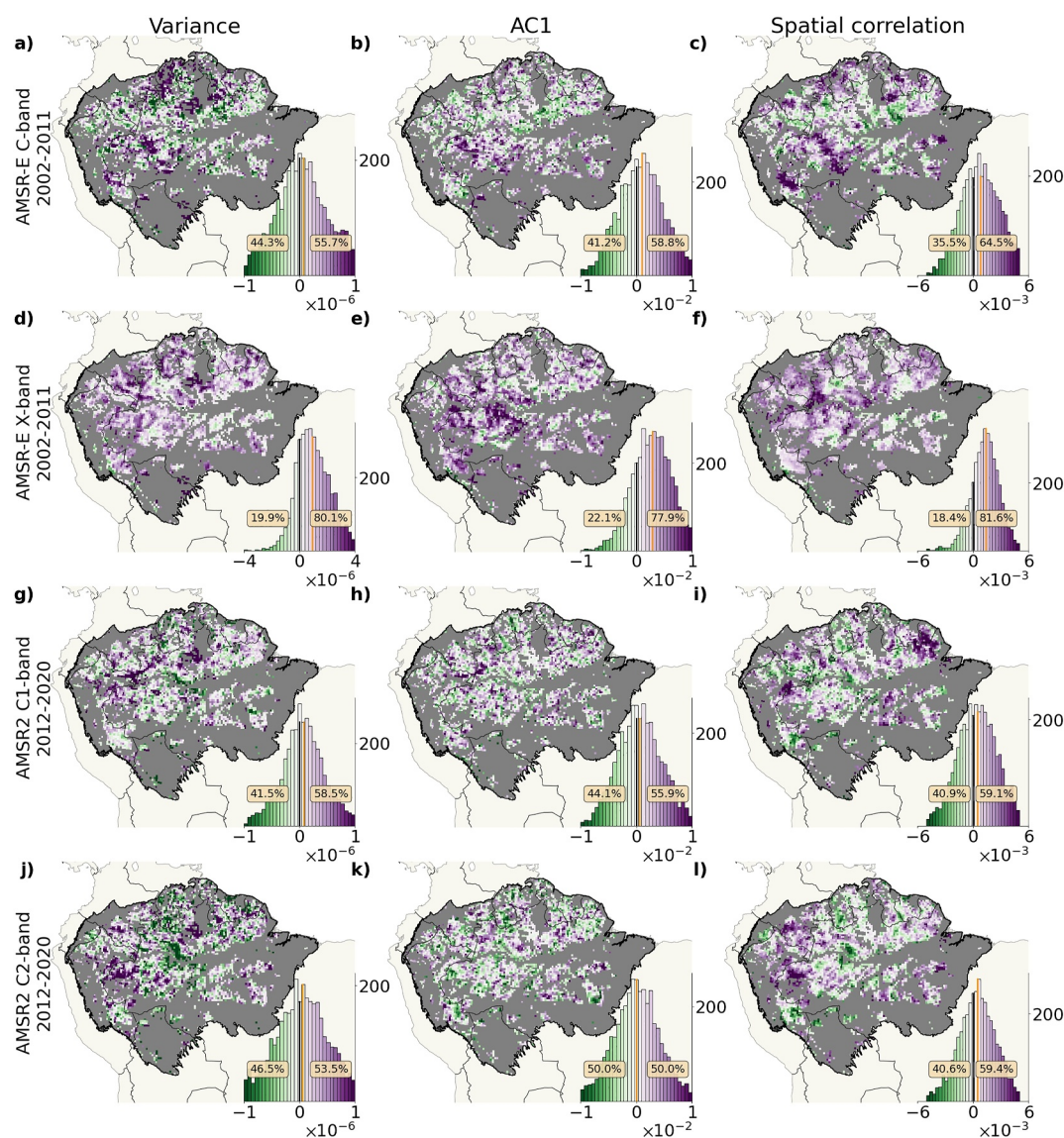
Figure 5. Changes in the different CSD indicators for the different Vegetation Optical Depth data sets. The change is assessed by linear trends of (a, d, g, j) variance, (b, e, h, k) AC1 and (c, f, i, l) spatial correlation as distributed across the whole Amazon basin based on (a)–(c) AMSR-E's C-band and (d)–(f) X-band for the years 2002–2011 and (g)–(i) AMSR2's C1-band and (j)–(l) and C2-band. The inlay histograms visualize the distribution of the trends with the same color-coding as on the maps. There, zero is marked by a black vertical line and the median of the distribution by an orange vertical line. Note that the colors and bins are restricted to suitable values.

indicators clearly increase over the period until around mid-2019. Interestingly, from then on until the end of the study period, all time series show a decrease, although the decrease in the spatial correlation is marginal compared to the previous increases. We restrict our study period to years before 2020 as the data for excluding human land use is not available thereafter, but using a less conservative analysis (see Text S10 in Supporting Information S1) we find that the indicators continue to decrease in the 2020-2022 period. However, this decrease could be explained by forest loss. Furthermore, AMSR2 also provides an X-band (10.7 GHz). The theory implies that it is less suitable for biomass assessment in the Amazon than the C-bands, but results on the X-band are discussed in Text S11 in Supporting Information S1.

All results are robust with respect to the parametrization of the STL de-trending method (Figures S3 and S4 in Supporting Information S1), the radius that defines the neighborhood (Figure S5 in Supporting Information S1),
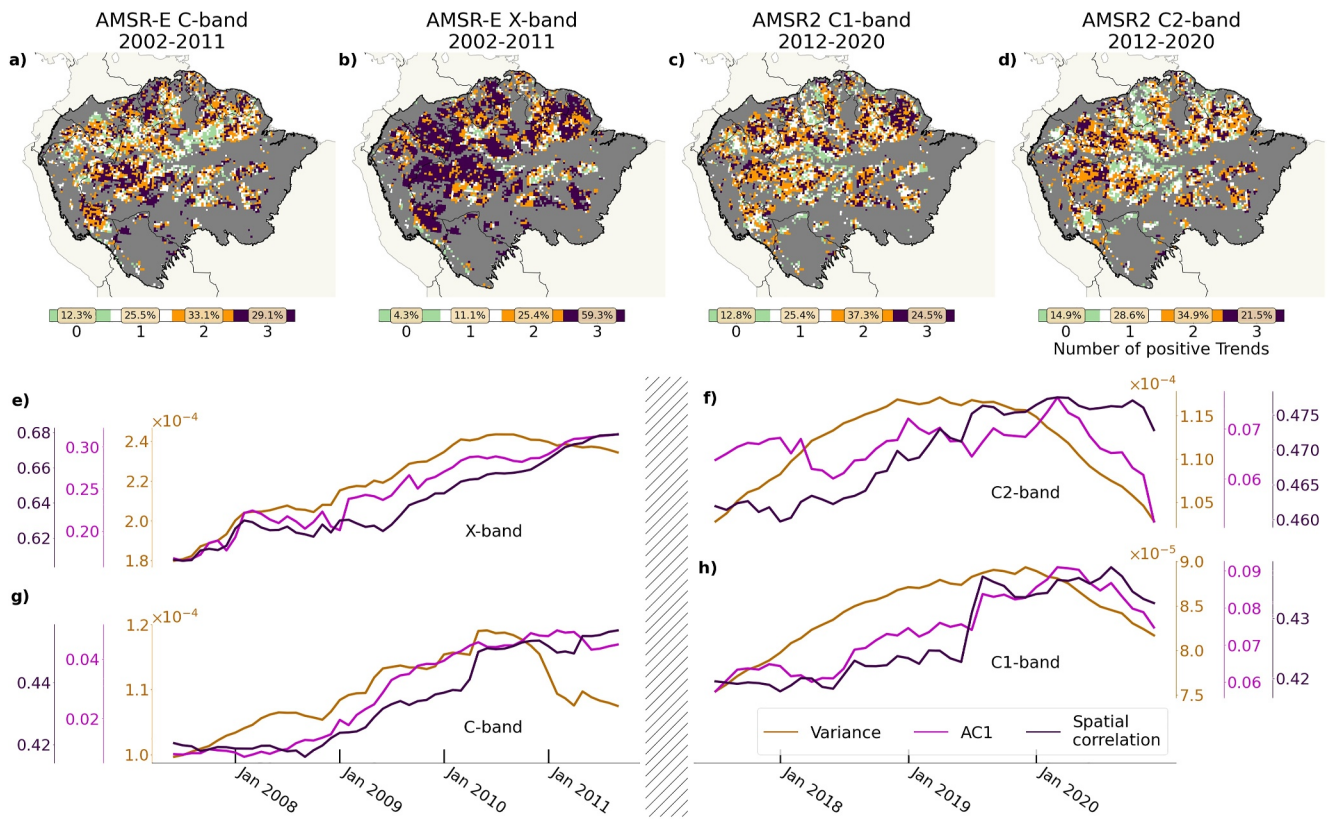
Figure 6. Resilience changes detected in the different Vegetation Optical Depth data sets. The assessment is based on (a, g) AMSR-E's C-band and (b, e) X-band as well as (c, h) AMSR2's C1-band and (d, f) C2-band. The maps in (a–d) summarize the results for the different CSD indicators by displaying the number of increasing indicators per grid cell, with the percentage of co-occurrences denoted below. The time series in (e–h) show the spatially averaged changes for each CSD indicator over the respective time period, allowing for an estimation of the overall resilience change of the vegetation in the Amazon basin as one ecosystem.

the size of the sliding windows (Figures S6 and S7 in Supporting Information S1), and the measure of increase in the indicator time series (Figures S8 and S9 in Supporting Information S1).

Even though they reveal a less dramatic picture of the condition of the Amazonian rainforest than that found by Boulton et al. (2022), these results confirm the resilience loss found in that work, which was based on the AC1 indicator and the merged data set VODCA analyzed from 1988 to 2016. In this work, we use a number of different indicators of CSD as well as different observations, which makes our results especially robust. In particular, for all data sets considered the number of cells where all three indicators show a positive trend is considerably larger than the expected number of 12.5% (=0.5^3), with 29.5% and 59.3% for AMSR-E's C- and X-band and 24.5% and 21.5% for AMSR2's C1- and C2-band, respectively (see also Figures 6a–6d).

4. Discussion

The ARF has been suggested as one of our planet's climate tipping elements (Lenton et al., 2008). We found signs of resilience loss in different data sets, but it must be discussed whether the detected changes in resilience are in fact due to the ARF losing stability. If the changes were merely artifacts, we see two potential reasons for that. First, the main factor affecting the ARF's vegetation and potential resilience changes is precipitation, which is decreasing due to deforestation and global warming. The South American monsoon system has recently been shown to be approaching a critical transition in response to the deforestation and forest degradation itself (Bochow & Boers, 2023). Thus, it is essential to ensure that the detected resilience changes in the vegetation's indicators of CSD are not just because of corresponding changes in precipitation statistics. In Text S12 in Supporting Information S1, we compare the sign of the trends of the CSD indicators between precipitation and vegetation. Even though Bochow and Boers (2023) find significant resilience loss of the

monsoon system in the southwest, Figure S17 in Supporting Information S1 indicates that the changes in the CSD indicators of vegetation are not likely to be a consequence of statistical changes in precipitation. Second, the detected losses of vegetation resilience could be artifacts of saturation, which they are not (Text S13 in Supporting Information S1). So, since the observed resilience losses do not appear to be artifacts, we now turn to possible drivers.

Interestingly, the regions in the southwest, where destabilization is detected in all data sets, correspond to the regions that are highly dependent on recycled moisture coming from the central and eastern Amazon. This implies that they are considerably spatially coupled, and in fact have been found to be more vulnerable to tipping (Wunderling et al., 2022). In addition, the results from the conceptual model show that spatial correlation gives an especially reliable indication of CSD in a highly coupled sub-system. In combination, this suggests that the spatial correlation can be considered a reliable indicator in the southwest Amazon. This is in line with our results, given that all data sets show increasing spatial correlation in parts of the southwestern Amazon. The reasons for the loss of vegetation resilience in the southwestern Amazon could be manifold. Several studies suggest that this region is especially susceptible to environmental changes in other parts of the Amazon basin. Deforestation upstream the wind trajectory can result in an abrupt decrease of water availability (Boers et al., 2017). In a deforestation experiment, Zemp, Schleussner, Barbosa, and Rammig (2017) detected the most severe reduction of precipitation in the southwestern Amazon, in particular during the dry season, and found the region to be at risk of propagated effects from deforestation in other parts. The conversion from rainforest to cropland has the largest negative impacts on dry season evaporated precipitation in the southwest as well as the northeast (Staal et al., 2020), coinciding with the two main regions of resilience loss detected in our analysis. All these studies link the vulnerability of the southwestern Amazon basin to the availability and demand of water. Thus, the increases in the CSD indicators could hint at a destabilization due to changes in incoming recycled moisture, which in return could be an effect of the high deforestation rates in the "arc of deforestation" further east, upstream the trade winds.

Hence, it is possible that the vegetation resilience loss is driven by moisture stress. As discussed in Text S14 in Supporting Information S1, the signs of CSD cannot always be explained by negative trends in precipitation. However, the lack of a negative trend in mean annual precipitation could still coincide with overall drying: in case of an increasing evapo-transpirative demand or, as many studies have suggested, shifts in the dry season length and strength, and increasing frequency of droughts that could be evened out by increases in precipitation during the rainy season or flood years (Marengo et al., 2018). In addition, the dry season length and intensity might affect vegetation resilience more directly than mean rainfall. For example, the drought in 2005 was concentrated around the southwest of the Amazon, and the drought in 2010 affected almost the entire south (Lewis et al., 2011; Marengo et al., 2008). It seems plausible that these droughts reduced the resilience in the southern and southwestern Amazon basin, and thus they might explain the pronounced loss of resilience that we detected in these regions. As discussed in Text S15 in Supporting Information S1, rising temperatures might contribute only slightly to the resilience loss. Thus, further work is needed to better understand the interplay of causes that can drive the ARF towards a dieback.

This work has focused on spatial correlation as an indicator of CSD, due to the spatially coupled structure of the ARF and the theoretical advantages this indicator shows in numerical experiments. Yet, multiple other potential (spatial) CSD indicators exist, such as spatial variance, spatial autocorrelation, spatial skewness (Dakos et al., 2010, 2011; Donangelo et al., 2010; Guttal & Jayaprakash, 2009), or spatial permutation entropy (Tirabassi & Masoller, 2023). Several of these would be applicable in this setting, but their thorough investigation and comparison was beyond the scope of this study. Still, a comparison of different spatial resilience indicators would improve our understanding of their applicability as well as their reliability to detect changes in resilience in the ARF, as well as in other spatially coupled ecosystems.

If we are to robustly capture resilience changes in the ARF, our efforts must be focused in a few key directions. First, long single-sensor time series are preferred to reliably trace the dynamics and potential resilience changes of vegetation ecosystems. Second, sensors and their derived VIs must be adequate to address the question of interest. To that end, it is important to find measures to assess the suitability of data sets. In the context of resilience analyses relying on small perturbations in detrended data, a sufficiently high signal-to-noise ratio is crucial. Furthermore, with respect to dense vegetation such as the ARF, it would be helpful to better understand problems

induced by saturation in the VIs on their higher order statistics (Smith & Boers, 2023). Finally, the applicability of indicators of CSD in different settings must be better understood, such that the most suitable approaches can be chosen depending on the system analyzed.

Overall, the complex changes we find in the ARF suggest that combining multiple data sets and indicators can give a clearer picture on the applicability of CSD, and the statistical robustness of trends in different parts of the Amazon. Our findings suggest that the previously found loss of resilience in the early 2000s (Boulton et al., 2022; Smith et al., 2022) can, in parts, be confirmed by our approach and data, with less distinct signals for the years 2012–2020. Nevertheless, we find a destabilization of the vegetation in the ARF since the beginning of the century, independent of the data source or the indicator of resilience change. This destabilization is especially pronounced in the southwestern Amazon basin.

5. Conclusions

We have shown, based on our conceptual model, that an increase in the average correlation of time series of a state variable in a cell with that of its neighbors, termed spatial correlations for simplicity, is an early and reliable indicator of resilience loss in spatially coupled systems. Since the model was set up to mimic the main coupling mechanism of the ARF and in particular the interaction of moisture and vegetation in the area, the indicator is applied to remotely sensed vegetation data for detecting resilience changes of the ARF. Additionally, the two classical indicators, variance and AC1, are employed to provide further robustness. The sensors AMSR-E and AMSR2 provide acceptably long VOD time series (2002–2011 and 2012–2020, respectively). For the early 2000s we find an overall increase of the CSD indicators, with more striking signs of resilience loss in AMSR-E's X-band. The spatial pattern is consistent across the two bands, with the largest losses of resilience occurring in the southwest and north. From 2012 to 2020, AMSR2's data reveals a less clear picture. Yet, the cells in the C1-band where all three indicators increase reside mostly in the northeast, coinciding with the resilience loss detected by AMSR-E in the preceding years. The cells that are likely undergoing destabilization according to AMSR2's C2-band are concentrated in the southwest.

Overall, even though the results differ somewhat for the individual data sets, we can conclude that the ARF's vegetation experienced a loss of resilience during the first two decades of the 21st century. More pronounced signals were found for the time period from 2002 to 2011, with the regions of destabilization comprising the western Amazon basin, the band along the northern boundary as well as the northeastern parts.

Conflict of Interest

The authors declare no conflicts of interest relevant to this study.

Data Availability Statement

The entire code used to produce the results of this study is published in Blaschke (2024). All data used in this study is publicly available. For this study, only cells within the Amazon basin (https://worldmap.maps.arcgis.com/home/item.html?id=f2c5f8762d1847fdbcc321716fb79e5a, accessed on 28 January 2021) are considered. Human Land Use is extracted from the MODIS Land Cover data set (Friedl & Sulla-Menashe, 2015) (MCD12C1, Version 6) available at https://lpdaac.usgs.gov/products/mcd12c1v006/ (accessed on 11 November 2021), based on Land Cover Type 1 in percent. The Hansen deforestation data (Hansen et al., 2013) was downloaded on 31 May 2022, from https://storage.googleapis.com/earthenginepartners-hansen/GFC-2021-v1.9/download.html. The VOD from AMSR-E (Vrije Universiteit Amsterdam (Richard de Jeu) and NASA GSFC (Manfred Owe), 2011) (LPRM-AMSR_E_L3_D_SOILM3_V002, C- and X-band) and AMSR2 (Vrije Universiteit Amsterdam (Richard de Jeu) and NASA GSFC (Manfred Owe), 2014) (LPRM-AMSR2_L3_D_SOILM3_V001, C1- and C2-band) can be found at https://hydro1.gesdisc.eosdis.nasa.gov/data/WAOB/LPRM_AMSRE_D_SOILM3.002 and https://hydro1.gesdisc.eosdis.nasa.gov/data/WAOB/LPRM_AMSR2_D_SOILM3.001/ and were last accessed on 8 November and 24 December 2022, respectively. The precipitation data from CHIRPS (Funk et al., 2015) is available at https://data.chc.ucsb.edu/products/CHIRPS-2.0/global_monthly/netcdf/ and was last accessed on 16 November 2022. It was downscaled to the same resolution as the VOD data by selecting only the grid cells matching VOD's grid cell centers (center of 5 × 5 cells).

References

Andela, N., Liu, Y. Y., van Dijk, A. I. J. M., de Jeu, R. A. M., & McVicar, T. R. (2013). Global changes in dryland vegetation dynamics (1988-2008) assessed by satellite remote sensing: Comparing a new passive microwave vegetation density record with reflective greenness data. *Biogeosciences*, *10*(10), 6657–6676. https://doi.org/10.5194/bg-10-6657-2013

Bathiany, S., Claussen, M., & Fraedrich, K. (2013a). Detecting hotspots of atmosphere–vegetation interaction via slowing down - Part 1: A stochastic approach. *Earth System Dynamics*, *4*(1), 63–78. https://doi.org/10.5194/esd-4-63-2013

Bathiany, S., Claussen, M., & Fraedrich, K. (2013b). Detecting hotspots of atmosphere–vegetation interaction via slowing down - Part 2: Application to a global climate model. *Earth System Dynamics*, *4*(1), 79–93. https://doi.org/10.5194/esd-4-79-2013

Ben-Yami, M., Skiba, V., Bathiany, S., & Boers, N. (2023). Uncertainties in critical slowing down indicators of observation-based fingerprints of the Atlantic Overturning Circulation. *Nature Communications*, *14*(1), 8344. https://doi.org/10.1038/s41467-023-44046-9

Blaschke, L. (2024). Spatial correlation increase in single-sensor satellite data reveals loss of Amazon rainforest resilience (v1.0.0). *Zenodo*. https://zenodo.org/doi/10.5281/zenodo.11519065

Bochow, N., & Boers, N. (2023). The South American monsoon approaches a critical transition in response to deforestation. *Science Advances*, *9*(40), eadd9973. https://doi.org/10.1126/sciadv.add9973

Boers, N. (2021). Observation-based early-warning signals for a collapse of the atlantic meridional overturning circulation. *Nature Climate Change*, *11*(8), 680–688. https://doi.org/10.1038/s41558-021-01097-4

Boers, N., Ghil, M., & Stocker, T. F. (2022). Theoretical and paleoclimatic evidence for abrupt transitions in the Earth system. *Environmental Research Letters*, *17*(9), 093006. https://doi.org/10.1088/1748-9326/ac8944

Boers, N., Marwan, N., Barbosa, H. M. J., & Kurths, J. (2017). A deforestation-induced tipping point for the South American monsoon system. *Scientific Reports*, *7*(1), 41489. https://doi.org/10.1038/srep41489

Boulton, C. A., Lenton, T. M., & Boers, N. (2022). Pronounced loss of Amazon rainforest resilience since the early 2000s. *Nature Climate Change*, *12*(3), 271–278. https://doi.org/10.1038/s41558-022-01287-8

Brando, P. M., Balch, J. K., Nepstad, D. C., Morton, D. C., Putz, F. E., Coe, M. T., et al. (2014). Abrupt increases in Amazonian tree mortality due to drought–fire interactions. *Proceedings of the National Academy of Sciences of the United States of America*, *111*(17), 6347–6352. https://doi.org/10.1073/pnas.1305499111

Brienen, R. J. W., Phillips, O. L., Feldpausch, T. R., Gloor, E., Baker, T. R., Lloyd, J., et al. (2015). Long-term decline of the Amazon carbon sink. *Nature*, *519*(7543), 344–348. https://doi.org/10.1038/nature14283

Brovkin, V., Bendtsen, J., Claussen, M., Ganopolski, A., Kubatzki, C., Petoukhov, V., & Andreev, A. (2002). Carbon cycle, vegetation, and climate dynamics in the Holocene: Experiments with the CLIMBER-2 model. *Global Biogeochemical Cycles*, *16*(4), 86-1–86-20. https://doi.org/10.1029/2001GB001662

Brovkin, V., Claussen, M., Petoukhov, V., & Ganopolski, A. (1998). On the stability of the atmosphere-vegetation system in the Sahara/Sahel region. *Journal of Geophysical Research*, *103*(D24), 31613–31624. https://doi.org/10.1029/1998JD200006

Brovkin, V., Ganopolski, A., & Svirezhev, Y. (1997). A continuous climate-vegetation classification for use in climate-biosphere studies. *Ecological Modelling*, *101*(2), 251–261. https://doi.org/10.1016/S0304-3800(97)00049-5

Chaparro, D., Piles, M., Vall-llossera, M., Camps, A., Konings, A. G., & Entekhabi, D. (2018). L-band vegetation optical depth seasonal metrics for crop yield assessment. *Remote Sensing of Environment*, *212*, 249–259. https://doi.org/10.1016/j.rse.2018.04.049

Cleveland, R. B., Cleveland, W. S., McRae, J. E., & Terpenning, I. (1990). STL: A seasonal-trend decomposition procedure based on LOESS. *Journal of Official Statistics*, *6*(1), 3–73. https://www.math.unm.edu/~lil/Stat581/STL.pdf

Dakos, V., Kéfi, S., Rietkerk, M., van Nes, E. H., & Scheffer, M. (2011). Slowing down in spatially patterned ecosystems at the brink of collapse. *The American Naturalist*, *177*(6), E153–E166. https://doi.org/10.1086/659945

Dakos, V., Scheffer, M., van Nes, E. H., Brovkin, V., Petoukhov, V., & Held, H. (2008). Slowing down as an early warning signal for abrupt climate change. *Proceedings of the National Academy of Sciences of the United States of America*, *105*(38), 14308–14312. https://doi.org/10.1073/pnas.0802430105

Dakos, V., van Nes, E. H., D'Odorico, P., & Scheffer, M. (2012). Robustness of variance and autocorrelation as indicators of critical slowing down. *Ecology*, *93*(2), 264–271. https://doi.org/10.1890/11-0889.1

Dakos, V., van Nes, E. H., Donangelo, R., Fort, H., & Scheffer, M. (2010). Spatial correlation as leading indicator of catastrophic shifts. *Theoretical Ecology*, *3*(3), 163–174. https://doi.org/10.1007/s12080-009-0060-6

DeArmond, D., Rovai, A., Suwa, R., & Higuchi, N. (2023). The challenges of sustainable forest operations in Amazonia. *Current Atherosclerosis Reports*, *10*(1), 77–88. https://doi.org/10.1007/s40725-023-00210-4

de Jeu, R. A. M., Wagner, W., Holmes, T. R. H., Dolman, A. J., van de Giesen, N. C., & Friesen, J. (2008). Global soil moisture patterns observed by space borne microwave radiometers and scatterometers. *Surveys in Geophysics*, *29*(4), 399–420. https://doi.org/10.1007/s10712-008-9044-0

Donangelo, R., Fort, H., Dakos, V., Scheffer, M., & Van Nes, E. H. (2010). Early warnings for catastrophic shifts in ecosystems: Comparison between spatial and temporal indicators. *International Journal of Bifurcation and Chaos in Applied Sciences and Engineering*, *20*(02), 315–321. https://doi.org/10.1142/S0218127410025764

Fan, L., Wigneron, J. P., Xiao, Q., Al-Yaari, A., Wen, J., Martin-StPaul, N., et al. (2018). Evaluation of microwave remote sensing for monitoring live fuel moisture content in the Mediterranean region. *Remote Sensing of Environment*, *205*, 210–223. https://doi.org/10.1016/j.rse.2017.11.020

Feldpausch, T. R., Phillips, O. L., Brienen, R. J. W., Gloor, E., Lloyd, J., Lopez-Gonzalez, G., et al. (2016). Amazon forest response to repeated droughts. *Global Biogeochemical Cycles*, *30*(7), 964–982. https://doi.org/10.1002/2015GB005133

Friedl, M., & Sulla-Menashe, D. (2015). MCD12C1 MODIS/Terra+Aqua land cover type yearly L3 global 0.05Deg CMG V006. *NASA EOSDIS Land Processes DAAC*. https://doi.org/10.5067/MODIS/MCD12C1.006

Funk, C., Peterson, P., Landsfeld, M., Pedreros, D., Verdin, J., Shukla, S., et al. (2015). The climate hazards infrared precipitation with stations—A new environmental record for monitoring extremes. *Scientific Data*, *2*(1), 150066. https://doi.org/10.1038/sdata.2015.66

Gatti, L. V., Basso, L. S., Miller, J. B., Gloor, M., Gatti Domingues, L., Cassol, H. L. G., et al. (2021). Amazonia as a carbon source linked to deforestation and climate change. *Nature*, *595*(7867), 388–393. https://doi.org/10.1038/s41586-021-03629-6

Gatti, L. V., Gloor, M., Miller, J. B., Doughty, C. E., Malhi, Y., Domingues, L. G., et al. (2014). Drought sensitivity of Amazonian carbon balance revealed by atmospheric measurements. *Nature*, *506*(7486), 76–80. https://doi.org/10.1038/nature12957

Gimeno, L., Dominguez, F., Nieto, R., Trigo, R., Drumond, A., Reason, C. J., et al. (2016). Major mechanisms of atmospheric moisture transport and their role in extreme precipitation events. *Annual Review of Environment and Resources*, *41*(1), 117–141. https://doi.org/10.1146/annurev-environ-110615-085558

Guttal, V., & Jayaprakash, C. (2009). Spatial variance and spatial skewness: Leading indicators of regime shifts in spatial ecological systems. *Theoretical Ecology*, *2*(1), 3–12. https://doi.org/10.1007/s12080-008-0033-1

Hansen, M. C., Potapov, P. V., Moore, R., Hancher, M., Turubanova, S. A., Tyukavina, A., et al. (2013). High-resolution global maps of 21st-century forest cover change. *Science*. https://doi.org/10.1126/science.1244693

Hawkins, E., & Sutton, R. (2012). Time of emergence of climate signals. *Geophysical Research Letters*, *39*(1), L01702. https://doi.org/10.1029/2011GL050087

Hirota, M., Holmgren, M., Van Nes, E. H., & Scheffer, M. (2011). Global resilience of tropical forest and savanna to critical transitions. *Science*, *334*(6053), 232–235. https://doi.org/10.1126/science.1210657

Hubau, W., Lewis, S. L., Phillips, O. L., Affum-Baffoe, K., Beeckman, H., Cuní-Sanchez, A., et al. (2020). Asynchronous carbon sink saturation in African and Amazonian tropical forests. *Nature*, *579*(7797), 80–87. https://doi.org/10.1038/s41586-020-2035-0

Huete, A., Didan, K., Miura, T., Rodriguez, E. P., Gao, X., & Ferreira, L. G. (2002). Overview of the radiometric and biophysical performance of the MODIS vegetation indices. *Remote Sensing of Environment*, *83*(1), 195–213. https://doi.org/10.1016/S0034-4257(02)00096-2

INPE. (2023). Terrabrasilis – Geographic data platform. Retrieved from http://terrabrasilis.dpi.inpe.br/en/home-page/

IPCC. (2022). *Climate change 2022: Mitigation of climate change: Working group III contribution to the sixth assessment Report of the intergovernmental panel on climate change* (P. R. Shuka, et al., Eds.). : Cambridge University Press. (OCLC: 1395516446)

Jackson, T. J., & Schmugge, T. J. (1991). Vegetation effects on the microwave emission of soils. *Remote Sensing of Environment*, *36*(3), 203–212. https://doi.org/10.1016/0034-4257(91)90057-D

Kirdiashev, K. P., Chukhlantsev, A. A., & Shutko, A. M. (1979). Microwave radiation of the Earth's surface in the presence of vegetation cover., *24*, 256–264.

Konings, A. G., Rao, K., & Steele-Dunne, S. C. (2019). Macro to micro: Microwave remote sensing of plant water content for physiology and ecology. *New Phytologist*, *223*(3), 1166–1172. https://doi.org/10.1111/nph.15808

Leite-Filho, A. T., de Sousa Pontes, V. Y., & Costa, M. H. (2019). Effects of deforestation on the onset of the rainy season and the duration of dry spells in southern Amazonia. *Journal of Geophysical Research: Atmospheres*, *124*(10), 5268–5281. https://doi.org/10.1029/2018JD029537

Lenton, T. M., Held, H., Kriegler, E., Hall, J. W., Lucht, W., Rahmstorf, S., & Schellnhuber, H. J. (2008). Tipping elements in the Earth's climate system. *Proceedings of the National Academy of Sciences of the United States of America*, *105*(6), 1786–1793. https://doi.org/10.1073/pnas.0705414105

Lewis, S. L., Brando, P. M., Phillips, O. L., van der Heijden, G. M. F., & Nepstad, D. (2011). The 2010 Amazon drought. *Science*, *331*(6017), 554. https://doi.org/10.1126/science.1200807

Lovejoy, T. E., & Nobre, C. (2018). Amazon tipping point. *Science Advances*, *4*(2), eaat2340. https://doi.org/10.1126/sciadv.aat2340

Lovejoy, T. E., & Nobre, C. (2019). Amazon tipping point: Last chance for action. *Science Advances*, *5*(12), eaba2949. https://doi.org/10.1126/sciadv.aba2949

Malhi, Y., Aragão, L. E. O. C., Galbraith, D., Huntingford, C., Fisher, R., Zelazowski, P., et al. (2009). Exploring the likelihood and mechanism of a climate-change-induced dieback of the Amazon rainforest. *Proceedings of the National Academy of Sciences of the United States of America*, *106*(49), 20610–20615. https://doi.org/10.1073/pnas.0804619106

Malhi, Y., Roberts, J. T., Betts, R. A., Killeen, T. J., Li, W., & Nobre, C. A. (2008). Climate change, deforestation, and the fate of the Amazon. *Science*, *319*(5860), 169–172. https://doi.org/10.1126/science.1146961

Marengo, J. A., Fisch, G. F., Alves, L. M., Sousa, N. V., Fu, R., & Zhuang, Y. (2017). Meteorological context of the onset and end of the rainy season in Central Amazonia during the GoAmazon2014/5. *Atmospheric Chemistry and Physics*, *17*(12), 7671–7681. https://doi.org/10.5194/acp-17-7671-2017

Marengo, J. A., Nobre, C. A., Tomasella, J., Oyama, M. D., Sampaio De Oliveira, G., De Oliveira, R., et al. (2008). The drought of Amazonia in 2005. *Journal of Climate*, *21*(3), 495–516. https://doi.org/10.1175/2007JCLI1600.1

Marengo, J. A., Souza, C. M., Thonicke, K., Burton, C., Halladay, K., Betts, R. A., et al. (2018). Changes in climate and land use over the Amazon region: Current and future variability and trends. *Frontiers in Earth Science*, *6*.https://www.frontiersin.org/article/10.3389/feart.2018.00228

Moesinger, L., Dorigo, W., de Jeu, R., van der Schalie, R., Scanlon, T., Teubner, I., & Forkel, M. (2020). The global long-term microwave vegetation optical depth climate archive (VODCA). *Earth System Science Data*, *12*(1), 177–196. https://doi.org/10.5194/essd-12-177-2020

Parry, I. M., Ritchie, P. D. L., & Cox, P. M. (2022). Evidence of localised Amazon rainforest dieback in CMIP6 models. *Earth System Dynamics*, *13*(4), 1667–1675. https://doi.org/10.5194/esd-13-1667-2022

Pascale, S., Carvalho, L. M. V., Adams, D. K., Castro, C. L., & Cavalcanti, I. F. A. (2019). Current and future variations of the monsoons of the Americas in a warming climate. *Current Climate Change Reports*, *5*(3), 125–144. https://doi.org/10.1007/s40641-019-00135-w

Phillips, O. L., Aragão, L. E. O. C., Lewis, S. L., Fisher, J. B., Lloyd, J., López-González, G., et al. (2009). Drought sensitivity of the Amazon rainforest. *Science*, *323*(5919), 1344–1347. https://doi.org/10.1126/science.1164033

Salati, E., Dall'Olio, A., Matsui, E., & Gat, J. R. (1979). Recycling of water in the Amazon Basin: An isotopic study. *Water Resources Research*, *15*(5), 1250–1258. https://doi.org/10.1029/WR015i005p01250

Samanta, A., Ganguly, S., Vermote, E., Nemani, R. R., & Myneni, R. B. (2012). Why is remote sensing of Amazon forest greenness so challenging? *Earth Interactions*, *16*(7), 1–14. https://doi.org/10.1175/2012EI440.1

Scheffer, M., Bascompte, J., Brock, W. A., Brovkin, V., Carpenter, S. R., Dakos, V., et al. (2009). Early-warning signals for critical transitions. *Nature*, *461*(7260), 53–59. https://doi.org/10.1038/nature08227

Smith, T., & Boers, N. (2023). Reliability of vegetation resilience estimates depends on biomass density. *Nature Ecology and Evolution*, 1–10. https://doi.org/10.1038/s41559-023-02194-7

Smith, T., Traxl, D., & Boers, N. (2022). Empirical evidence for recent global shifts in vegetation resilience. *Nature Climate Change*, *12*(5), 477–484. https://doi.org/10.1038/s41558-022-01352-2

Smith, T., Zotta, R.-M., Boulton, C. A., Lenton, T. M., Dorigo, W., & Boers, N. (2023). Reliability of resilience estimation based on multi-instrument time series. *Earth System Dynamics*, *14*(1), 173–183. https://doi.org/10.5194/esd-14-173-2023

Staal, A., Flores, B. M., Aguiar, A. P. D., Bosmans, J. H. C., Fetzer, I., & Tuinenburg, O. A. (2020). Feedback between drought and deforestation in the Amazon. *Environmental Research Letters*, *15*(4), 044024. https://doi.org/10.1088/1748-9326/ab738e

Staal, A., Tuinenburg, O. A., Bosmans, J. H. C., Holmgren, M., van Nes, E. H., Scheffer, M., et al. (2018). Forest-rainfall cascades buffer against drought across the Amazon. *Nature Climate Change*, *8*(6), 539–543. https://doi.org/10.1038/s41558-018-0177-y

Tian, F., Wigneron, J.-P., Ciais, P., Chave, J., Ogée, J., Peñuelas, J., et al. (2018). Coupling of ecosystem-scale plant water storage and leaf phenology observed by satellite. *Nature Ecology and Evolution*, *2*(9), 1428–1435. https://doi.org/10.1038/s41559-018-0630-3

Tirabassi, G., & Masoller, C. (2023). Entropy-based early detection of critical transitions in spatial vegetation fields. *Proceedings of the National Academy of Sciences of the United States of America*, *120*(1), e2215667120. https://doi.org/10.1073/pnas.2215667120

Vogel, M. M., Hauser, M., & Seneviratne, S. I. (2020). Projected changes in hot, dry and wet extreme events' clusters in CMIP6 multi-model ensemble. *Environmental Research Letters*, *15*(9), 094021. https://doi.org/10.1088/1748-9326/ab90a7

Vreugdenhil, M., Dorigo, W. A., Wagner, W., de Jeu, R. A. M., Hahn, S., & van Marle, M. J. E. (2016). Analyzing the vegetation parameterization in the TU-Wien ASCAT soil moisture retrieval. *IEEE transactions on geoscience and remote sensing* (Vol. 54(6), pp. 3513–3531). https://doi.org/10.1109/TGRS.2016.2519842

Vrije Universiteit Amsterdam (Richard de Jeu) and NASA GSFC (Manfred Owe). (2011). *AMSR-E/Aqua surface soil moisture (LPRM) L3 1 day 25 km x 25 km descending V002*. Goddard Earth Sciences Data and Information Services Center (GES DISC). https://doi.org/10.5067/MXL0MFDHWP07

Vrije Universiteit Amsterdam (Richard de Jeu) and NASA GSFC (Manfred Owe). (2014). *AMSR2/GCOM-W1 surface soil moisture (LPRM) L3 1 day 25 km x 25 km descending V001*. Goddard Earth Sciences Data and Information Services Center (GES DISC). https://doi.org/10.5067/CGDEOBASZ178

Wang, H., Ciais, P., Sitch, S., Green, J. K., Tao, S., Fu, Z., et al. (2024). Anthropogenic disturbance exacerbates resilience loss in the Amazon rainforests. *Global Change Biology*, *30*(1), e17006. https://doi.org/10.1111/gcb.17006

Wunderling, N., Staal, A., Sakschewski, B., Hirota, M., Tuinenburg, O. A., Donges, J. F., et al. (2022). Recurrent droughts increase risk of cascading tipping events by outpacing adaptive capacities in the Amazon rainforest. *Proceedings of the National Academy of Sciences of the United States of America*, *119*(32), e2120777119. https://doi.org/10.1073/pnas.2120777119

Wuyts, B., & Sieber, J. (2023). Emergent structure and dynamics of tropical forest-grassland landscapes. *Proceedings of the National Academy of Sciences of the United States of America*, *120*(45), e2211853120. https://doi.org/10.1073/pnas.2211853120

Zemp, D. C., Schleussner, C.-F., Barbosa, H. M. J., Hirota, M., Montade, V., Sampaio, G., et al. (2017). Self-amplified Amazon forest loss due to vegetation-atmosphere feedbacks. *Nature Communications*, *8*(1), 14681. https://doi.org/10.1038/ncomms14681

Zemp, D. C., Schleussner, C.-F., Barbosa, H. M. J., & Rammig, A. (2017). Deforestation effects on Amazon forest resilience: Deforestation effects. *Geophysical Research Letters*, *44*(12), 6182–6190. https://doi.org/10.1002/2017GL072955